Noname manuscript No.
(will be inserted by the editor)

Numerical continuation analysis of a three-dimensional aircraft main landing gear mechanism

J. A. C. Knowles · B. Krauskopf · M. Lowenberg

Received: date / Accepted: date

Abstract A method of investigating quasi-static landing gear mechanisms is presented and applied to a three-dimensional aircraft main landing gear mechanism model. The model has 19 static equilibrium equations and 20 equations describing the geometric constraints in the mechanism. In the spirit of bifurcation analysis, solutions to these 39 steady-state equations are found and tracked, or continued, numerically in parameters of interest. A design case-study is performed on the landing gear actuator position to demonstrate the potential relevance of the method for industrial applications. The trade-off between maximal efficiency and peak actuator force reduction when positioning the actuator is investigated. It is shown that the problem formulation is very flexible and allows actuator force, length and efficiency information to be obtained from a single numerical continuation computation with minimal data post-processing. The study suggests that numerical continuation analysis has potential for investigating even more complex landing gear mechanisms, such as those with more than one sidestay.

Keywords Landing Gear · Bifurcation analysis · Numerical continuation

The research of J. A. C. Knowles was supported by an Engineering and Physical Sciences research council CASE award in collaboration with Airbus

J. A. C. Knowles
Faculty of Engineering, Queen's Building, University Walk, Bristol, BS8 1TR, UK

B. Krauskopf
Department of Mathematics, The University of Auckland, Private Bag 92019, Auckland 1142, New Zealand

M. Lowenberg
Faculty of Engineering, Queen's Building, University Walk, Bristol, BS8 1TR, UK

1 Introduction

The landing gears on an aircraft are used to transfer ground loads during take-off, landing and taxiing, into the structural elements of the fuselage and wing. Until the late 1920s, landing gears were structural elements that either remained attached to the aircraft, protruding during flight as on the ground, or were ditched upon take-off to reduce weight and drag but leaving the pilot to await an uncomfortable landing [1]. These rather inelegant solutions were soon superceded by retractable landing gears, which offered the drag reduction benefits of the detachable gears alongside the landing comfort associated with keeping the gears attached to the aircraft, for the price of a (small) weight penalty.

Current civil airliners all use retractable landing gear mechanisms for their nose landing gear (NLG) and main landing gears (MLG). These designs vary from aircraft to aircraft, but there are some standard features of landing gear mechanisms that are present on all modern civil airliners. For a sketch of a typical single-sidestay MLG configuration see Figure 1. The main structural element of the landing gear is the shock strut. It is responsible for absorbing vertical loads on touchdown, and for reducing the vibrations experienced in the cabin when the aircraft is in motion on the ground. One end of the shock strut is connected to the wing, with the opposite end holding the wheel assembly. The shock strut is supported by a sidestay when in the deployed position, which transfers loads acting perpendicular to the shock strut axis into the airframe. As the mechanism must be able to move between the deployed and retracted states, this sidestay is required to fold; the sidestay therefore comprises an upper sidestay link attached to the airframe at one end, joined to a lower sidestay link attached to the shock strut. At or near

the folding point between the upper and lower sidestay links, a pair of locklinks are used to fix the two sidestay links to be in line when the MLG is deployed. These locklinks keep the landing gear locked in the deployed position, and they must be unlocked before the retraction cycle commences.

For some landing gears, the retraction mechanism is able to operate in a fixed plane; NLG mechanisms are typical examples of such planar landing gear mechanisms. These landing gears can be modelled mathematically in a planar co-ordinate system, reducing the complexity of their mathematical description. Many landing gears however, and in particular the MLG on practically all current civil airliners, do not retract in a fixed plane. These landing gears are stowed in the wing root/fuselage intersection, where limited stowage height within the wing prohibits the possibility of retracting in a planer manner. It is therefore necessary for the sidestays and locklinks of the MLG to rotate out of the retraction plane whilst the gear retracts or deploys. This allows the mechanism to lie flat in the body of the aircraft when retracted, requiring a minimal amount of space to stow the gear. The three-dimensional nature of the MLG mechanism implies that the mechanism cannot be described within a single planar co-ordinate system; hence the approach adopted here is to model the mechanism in terms of two rotational planes – a global plane in which the shock strut rotates and a local plane in which the sidestays and locklinks rotate; the latter plane itself moves as a function of the shock strut position.

Irrespective of how the landing gear mechanism operates, it requires some form of energy input to move between the deployed and retracted state. This energy is provided by the retraction actuator. The retraction actuator must achieve a smooth transition between the deployed and retracted states to maximise the structural life of the aircraft and maintain passenger comfort, whilst operating as efficiently as possible without adding an excessive amount of weight to the aircraft. It must also provide enough energy to overcome the landing gear weight and any aerodynamic forces (such as drag) which may be working against the retracting gear. In the NLG previously considered in [2], both aerodynamic drag and structural weight worked in the NGL retraction plane in a manner that aided the actuator motion when extending the gear, but opposed the retraction motion. For a MLG the aerodynamic drag does not have such a large effect on the landing gear extension and retraction, because a MLG main strut usually moves in a plane perpendicular to the onset flow. This means that when the aircraft is flying directly into the flow with zero sideslip there is no drag force acting in the MLG shock strut retraction plane. On the other hand, when the aircraft is sideslipping during landing or takeoff, the drag component in the retraction plane may either aid or oppose a retracting MLG (depending on which direction the aircraft is sideslipping).

The challenge of designing a landing gear can be tackled in different ways, each chosen depending on varying requirement levels of complexity and accuracy. Geometric analysis methods are often used during preliminary design to size the landing gear [3], whilst full dynamic multibody simulations are generally used for more detailed design purposes later on in the design process. There is, however, largely an absence of intermediate level methods in the literature on landing gear modelling: when analytical methods become too complicated to be implemented easily, the aircraft designer will generally resort to using dynamic simulations, creating and analysing a model with conventional industrial-standard multi-body simulation software such as ADAMS or Dymola. Whilst these models have the capacity to provide very accurate replications of reality, the time requirements to create, validate and run these models suggests that there is considerable potential for complementary analysis approaches.

The complementary approach presented here makes use of concepts from the theory of dynamical systems; see [4–6] for background information. Several recent applications of dynamical systems methods have demonstrated the advantages that they can offer in an aerospace context; this includes the analysis of aircraft ground dynamics [7,8], the study of nose landing gear shimmy [9] and NLG mechanism modelling [2]. To be able to use these dynamical systems methods for analysing landing gear mechanisms, the mechanism configuration and internal force distribution is formulated as a system of coupled equations, which are inherently nonlinear due to various geometric constraints. The steady-state solutions of these equations can then be found and followed, or continued, in parameters of interest with standard numerical continuation software, such as AUTO [10] or, as is used for this research, the Dynamical Systems Toolbox extension for MATLAB [11]. A particular advantage of this coupled-equation approach is that solutions can be continued in phase and parameter space without the need to reformulate the governing equations as a function of specific parameters under consideration. This approach to the equation formulation also allows for a convenient analysis of different landing gear configurations, as the model is fully parameterised. The advantage of this over traditional simulations is that the same model (with new parameter values) can be used for any number of different landing gear configurations.

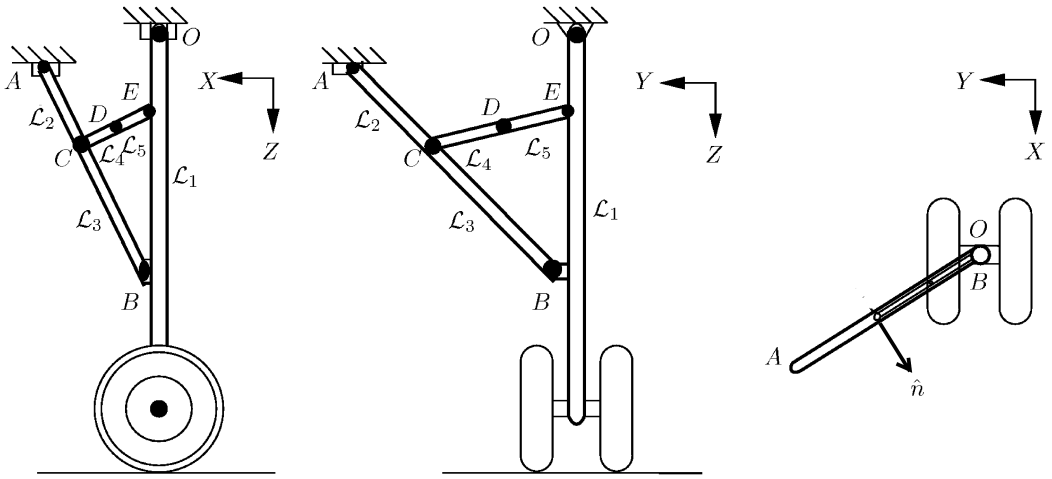

Fig. 1: Plan views of the single sidestay MLG; axes denote the positive directions of the global (X,Y,Z) co-ordinate system, whose origin is at the shock strut attachment point O.

The method is demonstrated with a case study into the effect of the landing gear retraction/extension actuator placement on actuator performance. Three measures of actuator performance are considered: peak force, efficiency and actuator length change. All of these measures are obtained with minimal post-processing of the numerical continuation data and can, hence, be used directly to inform design decisions. These results are compared to those obtained analytically for a simplified geometric actuator model. A general agreement between the two sets of results is demonstrated, which validates the numerical continuation study, but the limitations of the geometric model highlight the scope and suitability of numerical continuation as a tool to analyse complex landing gear mechanisms.

The paper is organised as follows. Section 2 describes the landing gear model used in the continuation analysis, leading on to the retraction actuator case study investigation of this model presented in Section 3. The analysis of the simplified geometric model is presented in Secton 3.6, and future avenues for MLG modelling and analysis can be found in Section 4.

2 Single-Sidestay MLG Mechanism Model

The single sidestay MLG considered here consists of five links; they are assumed to be rigid bodies with uniformly distributed mass along their lengths. Each link, $\mathcal{L}_i$, is connected to another link or the aircraft structure via rotational joints; joints C, D, E and O are planar joints, whilst joints A and B are spherical joints that allow connected bodies to rotate about the joint freely in three-dimensions. Figure 1 shows the global landing gear co-ordinate system, with capital letters used throughout to denote global position co-ordinates and rotations. For simplicity, the X-axis is defined as the shock strut rotation axis, with the shock strut rotation joint at the global co-ordinate origin point O. The gear retracts in the positive Y-direction and the Z-axis is aligned with the global gravity vector, positive down. The landing gear shock strut rotation is therefore confined to the global (Y, Z)-plane throughout the retraction cycle. Note that this choice of global co-ordinate system is chosen to align closely with the convention for aircraft body axes, where the X-axis is along the body of the aircraft (roll axis) positive from c/g to nose, the Z-axis (yaw axis) positive down and the Y-axis (pitch axis) defined to create a right-handed co-ordinate system. These co-ordinates were chosen to facilitate transforming landing gear points given in aircraft body axes to the global co-ordinates used here.

The local sidestay rotation plane is defined by points A, O and B from Figure 1. Vector $\overline{OA}$ is assumed fixed in the global co-ordinate system, and vector $\overline{OB}$ is defined as a function of the global shock strut rotation angle θ_1 because points O and B are fixed relative to the shock strut. The normal vector to the sidestay rotation plane is therefore

$$\hat{n} = \overline{OB} \times \overline{OA}\,. \tag{1}$$

The sidestay local co-ordinate system can now be defined with a rotation matrix T about the global origin

point O, that aligns the local x-axis with $\hat{n}$ by a rotation over α about the global Y-axis followed by a rotation through β about the intermediate z-axis:

$$T = \begin{bmatrix} \cos\beta\cos\alpha & -\sin\beta & \cos\beta\sin\alpha \\ \sin\beta\cos\alpha & \cos\beta & \sin\beta\sin\alpha \\ -\sin\alpha & 0 & \cos\alpha \end{bmatrix} . \quad (2)$$

Lower case letters are used throughout to denote local position co-ordinates and rotations, such that local and global co-ordinates can be related by

$$\begin{bmatrix} x \\ y \\ z \end{bmatrix} = T \begin{bmatrix} X \\ Y \\ Z \end{bmatrix} . \quad (3)$$

The (y, z)-plane in the transformed co-ordinates is the sidestay rotation plane, obtained by applying the transformation matrix T to the global co-ordinates. The sidestays (links $\mathcal{L}_2$ and $\mathcal{L}_3$) and locklinks (links $\mathcal{L}_4$ and $\mathcal{L}_5$) are constrained to rotate in this transformed plane, and as such their geometric constraints are formulated in local co-ordinates. The shock strut (link $\mathcal{L}_1$) is constrained to rotate about the global X-axis, described in terms of global co-ordinates.

The equations are formulated by considering each link $\mathcal{L}_i$ within the mechanism as an individual rigid body in static equilibrium. This method has been used in previous work to study planar mechanisms, and was shown to provide equivalent results to those obtained with a multibody dynamic simulation software package [2]. The challenge for a three-dimensional landing gear is to provide a convenient formulation and implementation of the planar constraints between the sidestays and locklinks in three-dimensional space. The solution adopted here is to constrain the sidestays to lie in a local plane defined by the main fitting and sidestay attachment point position. The geometric constraints can then be implemented in the same way as for the planar mechanisms in previous work, with the additional constraint that the x-co-ordinate of the transformed elements be zero throughout.

2.1 Link description and co-ordinate systems

Figure 2 depicts the general naming convention used for each link within the landing gear mechanism in local co-ordinates. Each link is described in terms of seven elements, $\mathcal{L}_i = \{X_i, Y_i, Z_i, \hat{n}, \theta_i, L_i, m_i\}$, where:

- $\mathcal{L}_i$ is the i^{th} link;
- X_i, Y_i, Z_i are the global Cartesian co-ordinates which describe the position of $\mathcal{L}_i$'s centre of gravity (cg);

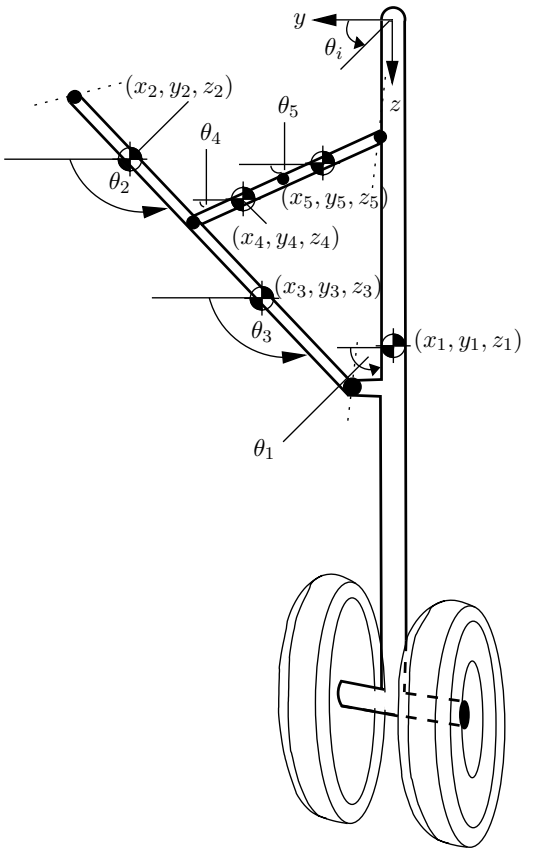

Fig. 2: Mechanism expressed in local co-ordinates, as viewed along the normal vector to the sidestay plane.

- $\hat{n}$ is the normal vector to $\mathcal{L}_i$'s plane of rotation, i.e. out of the page in Figure 2;
- θ_i is the local rotation of $\mathcal{L}_i$ relative to the local y-axis[1];
- L_i is the length of $\mathcal{L}_i$;
- m_i is the mass of $\mathcal{L}_i$, assumed to be evenly distributed along $\mathcal{L}_i$.

Each link is also acted upon by several forces. These forces can be expressed in global or local co-ordinates which are related via the transformation matrix T as:

$$\begin{bmatrix} F^x \\ F^y \\ F^z \end{bmatrix} = T \begin{bmatrix} \mathcal{F}^X \\ \mathcal{F}^Y \\ \mathcal{F}^Z \end{bmatrix} . \quad (4)$$

The left-hand side of Equation (4) is the local (x,y,z) projection of the given force, with the symbol F used to distinguish the force as being in local co-ordinates; the right-hand side of the equation contains the global

[1] For the main strut $\mathcal{L}_1$ a global rotation Θ_1 is used to define the link. The corresponding local rotation θ_1 is a function of Θ_1

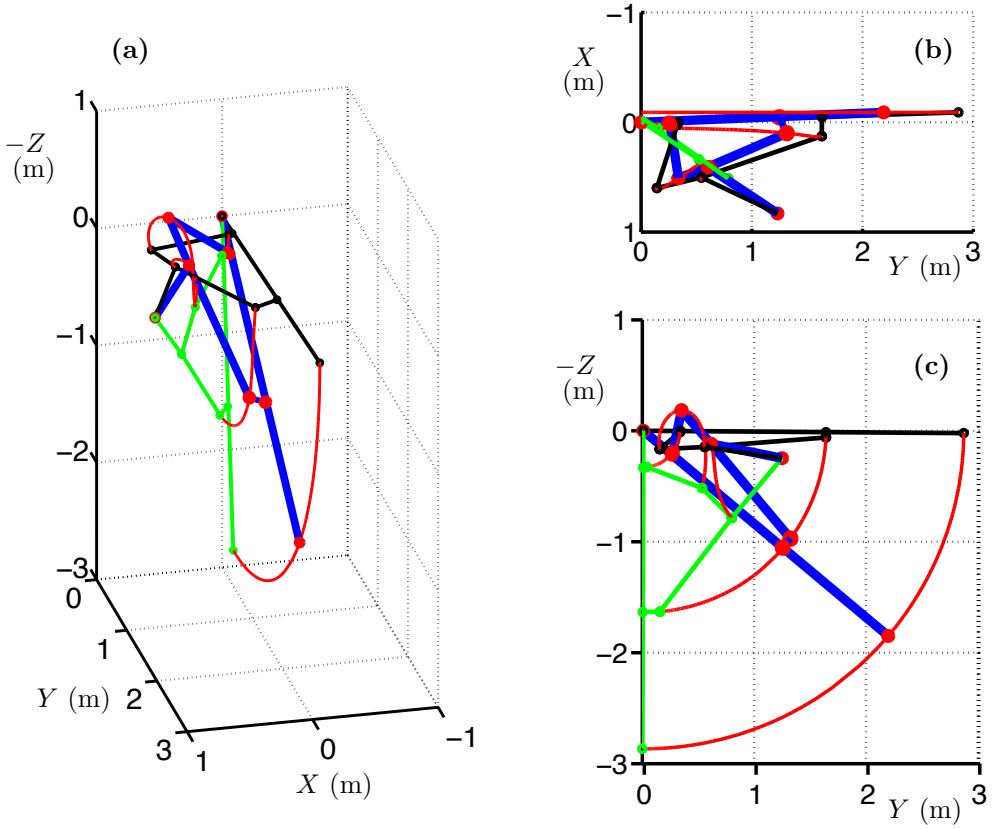

Fig. 3: The 3D main landing gear at three different points in its retraction cycle; deployed (green), mid-cycle (blue) and retracted (black). Shown as a 3D view in (a), a top view ((X,Y)-plane) in (b) and a side view ((Y,Z)-plane) in (c). Red curves indicate rotational joint traces.

(X,Y,Z) projections of the same force, denoted by the symbol $\mathcal{F}$ to distinguish it as being a global force projection. A subscript naming convention is used to uniquely identify the forces exerted on the i^{th} link by other links attached to it; this convention is introduced in Section 2.3 where the force balance equations are presented.

2.2 Geometric constraints

A system of 19 geometric constraint equations is needed to express the physical constraints in the landing gear mechanism; of these, 16 equations are formulated in the local sidestay co-ordinate cg positions (x_i, y_i, z_i), along with a single rotation θ_i as defined in Figure 2. The remaining three equations are expressed in global co-ordinates $(X_i, Y_i, Z_i, \Theta_i)$, such that the 19 geometric constraint equations obtained are:

$$\begin{bmatrix} x_2 \\ y_2 - \frac{L_2}{2}\cos(\theta_2) - A^y \\ z_2 - \frac{L_2}{2}\sin(\theta_2) - A^z \\ x_3 \\ y_2 - y_3 + \frac{L_2}{2}\cos(\theta_2) + \frac{L_3}{2}\cos(\theta_3) \\ z_2 - z_3 + \frac{L_2}{2}\sin(\theta_2) + \frac{L_3}{2}\sin(\theta_3) \\ y_3 - y_1 + \frac{L_3}{2}\cos(\theta_3) + l_{13}\cos(\theta_1 + \omega_1) \\ z_3 - z_1 + \frac{L_3}{2}\sin(\theta_3) + l_{13}\sin(\theta_1 + \omega_1) \\ X_1 \\ Y_1 - \frac{L_1}{2}\cos(\Theta_1) \\ Z_1 - \frac{L_1}{2}\sin(\Theta_1) \\ x_4 \\ y_4 - y_2 - \frac{L_2}{2}\cos(\theta_2) + \frac{L_4}{2}\cos(\theta_4) \\ z_4 - z_2 - \frac{L_2}{2}\sin(\theta_2) + \frac{L_4}{2}\sin(\theta_4) \\ x_5 \\ y_5 - y_4 + \frac{L_5}{2}\cos(\theta_5) + \frac{L_4}{2}\cos(\theta_4) \\ z_5 - z_4 + \frac{L_5}{2}\sin(\theta_5) + \frac{L_4}{2}\sin(\theta_4) \\ y_5 - y_1 + \frac{L_5}{2}\cos(\theta_5) - l_{15}\cos(\theta_1 + \omega_2) \\ z_5 - z_1 + \frac{L_5}{2}\sin(\theta_5) - l_{15}\sin(\theta_1 + \omega_2) \end{bmatrix} = 0\,. \quad (5)$$

Here A^y and A^z are the local co-ordinate y- and z-components of the sidestay attachment point (point A in Figure 1), l_{13} and l_{15} are the lengths from the shock strut cg to the adjoining ends of links $\mathcal{L}_3$ and $\mathcal{L}_5$ respectively, and ω_1 and ω_2 are the angles l_{13} and l_{15} make with the shock strut centreline (in local co-ordinates). All other symbols follow the naming convention as described in Section 2.1, with capital letters indicating global co-ordinates and lower cases indicating local co-ordinates.

The above system of 19 equations is described in terms of 20 link positional states (X_i,Y_i,Z_i,θ_i for $i \in \mathbb{Z} = [1, 5]$); therefore, if one of the 20 states is specified, the other 19 states can be determined uniquely. This can be used to plot the relation between different positional states, or the states can be used to plot the configuration of the landing gear at various points throughout the retraction cycle. Figure 3 was created from a continuation run using just the geometric states and constraints from Equation (5). It shows the landing gear in three positions; deployed (but unlocked) in green, semi-retracted ($\Theta_1 = 40°$) in blue and fully retracted in black. In Figure 3(a) the landing gear is viewed in 3D. Dots are used to indicate the mechanism joint positions for each of the links, with red lines tracing out the joint positions for the five links as the gear moves from the deployed to retracted state.

The two projections in Figure 3(b) and 3(c) provide a sense of the three-dimensional nature of the mechanism. Considering the deployed gear depicted in green, all of the links can be viewed clearly in the (Y, Z) plane shown in Figure 3(c), but looking down on the gear in Figure 3(b) the sidestay and locklinks appear to be on top of each other. This is because the shock strut sits (approximately) vertically in the deployed position, so the sidestay rotation plane (which is a function of shock strut angle) is also vertical when the gear is deployed. As the gear retracts, the sidestay plane rotates so that, when the gear is viewed around the midway point in the retraction cycle (blue gear, in Figure 3), all links are clearly visible in projections Figure 3(b) and 3(c). As the landing gear retracts further, the sidestay plane becomes more horizontal until $\Theta_1 = 10°$ when the links end up in their 'most horizontal' state (i.e. they are viewed as a single line in a side view). In the fully retracted state for $\Theta_1 = 0°$ (the black gear in Figure 3) the sidestay plane has rotated more than 90° from the deployed state so the gear does not appear as a single line in Figure 3(c). This large rotation that the sidestay plane experiences is the main reason why the red joint traces between the sidestay links and locklinks in Figure 3 are non-circular.

2.3 Force and Moment Equilibrium Equations

The 19 geometric constraints are supplemented with a second set of 19 equations that describe the force and moment equilibrium necessary for the gear to be in a steady-state. For the whole MLG to be in equilibrium, each of the five links must be in force and moment equilibrium and the joints must be in force equilibrium. The general equilibrium cases are discussed below.

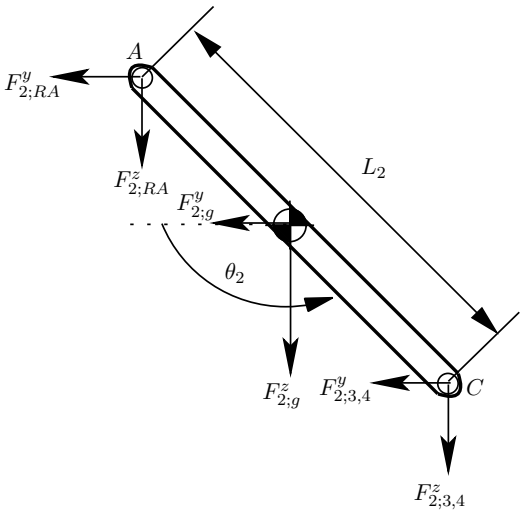

Fig. 4: Free-body diagram of link $\mathcal{L}_2$ in local co-ordinates.

Figure 4 shows a free-body diagram for the upper sidestay link $\mathcal{L}_2$ in the sidestay rotation plane. It is representative of all links in local co-ordinates, that is, for the lower sidestay link ($\mathcal{L}_3$) and the locklinks ($\mathcal{L}_4$ and $\mathcal{L}_5$); the specific case for the shock strut is considered later. In the general case, there are two types of forces which act on the link: the externally created forces due to gravity or drag, and the resultant internal forces transferred by links joined to link $\mathcal{L}_2$. These forces are denoted by $F_{i;*}$ in the general case, where the subscript i denotes the link number that the force is acting on and the subscript $*$ denotes the element exerting that force on $\mathcal{L}_i$ which can be:

- the in-plane gravitational force acting on the body – $m_i g$,
- the internal force applied by an adjoining link(s) – $F_{i;*}$ – where the link number appears in place of the symbol $*$,
- the internal force between the strut and the aircraft body, either RA for the reaction force at point A or RO for the reaction force at point O.

The superscripts denote the component of that force in the local co-ordinate directions. From Figure 4, the force denoted by $F^y_{2;RA}$ can therefore be interpreted as being the local y-component of the force exerted on $\mathcal{L}_2$ by the aircraft body at point A, whereas $F^z_{2;3,4}$ is the local z-component of the force exerted on $\mathcal{L}_2$ by the adjoining links, $\mathcal{L}_3$ and $\mathcal{L}_4$.

Within the sidestay plane, for an arbitrary link $\mathcal{L}_i$ to be in static equilibrium the sum of the forces acting on the link must equal zero. Using the notation conventions introduced before, this means that:

$$\sum_* F^y_{i;*} = 0\,, \tag{6a}$$

$$\sum_* F^z_{i;*} = 0\,. \tag{6b}$$

The forces depicted in Figure 4 are acting in the chosen positive direction, which aligns with the positive local (y, z) co-ordinate directions. For the specific case of $\mathcal{L}_2$, Equations (6a)–(6b) become:

$$\sum_* F^y_{2;*} = F^y_{2;RA} + F^y_{2;g} + F^y_{2;3,4} = 0\,, \tag{7a}$$

$$\sum_* F^z_{2;*} = F^z_{2;RA} + F^z_{2;g} + F^z_{2;3,4} = 0\,. \tag{7b}$$

The sum of the moments about any given point P along the link must also be zero. Since the moments are created by forces, it is convenient to use a similar subscript naming convention as used above for the forces themselves, with a slight change in the meaning of the superscript: it now denotes the point in the sidestay rotation plane about which moments are taken, and length $l^P_{i;*}$ is the moment arm of force $F_{i;*}$. The general expression for this moment equilibrium condition therefore is:

$$\sum_* M^P_{i;*} = l^P_{i;*} F_{i;*} = 0\,. \tag{8}$$

Point P can be chosen arbitrarily, but to simplify the moment equilibrium expression as much as possible P is chosen at joint A for link 2 (see Figure 4), so that the forces acting at that end of the link do not have to be included in the moment equilibrium expression.

Counter-clockwise moments are taken to be positive, as this reflects the positive rotation sign convention used in the local co-ordinate system. As the links are assumed to be homogenous, the gravitational force acts at the geometric midpoint of the i^{th} link; this leads to the following expression for the moment equilibrium equation of $\mathcal{L}_2$:

$$\begin{aligned}\textstyle\sum_* M^A_{1;*} = {} & L_2 \sin(\theta_2)(F^y_{2;3,4} + \tfrac{1}{2}F^y_{2;g}) \\ & + L_2 \cos(\theta_2)(F^z_{2;3,4} + \tfrac{1}{2}F^z_{2;g}) = 0\,.\end{aligned} \tag{9}$$

Further constraints are applied by enforcing the 'equilibrium of joints' condition in between joined elements. For $\mathcal{L}_2$, no links are joined at point A, but both $\mathcal{L}_3$ and $\mathcal{L}_4$ are joined to $\mathcal{L}_2$ at point C so the sum of all internal joint forces at point C must be zero for the mechanism to be in static equilibrium. The resulting force equilibrium equations at joint C are therefore:

$$F^y_{2;3,4} + F^y_{3;2,4} + F^y_{4;2,3} = 0\,, \tag{10a}$$

$$F^z_{2;3,4} + F^z_{3;2,4} + F^z_{4;2,3} = 0\,. \tag{10b}$$

Equations (7), (9) and (10) are supplemented with equivalent equations for $\mathcal{L}_3$, $\mathcal{L}_4$ and $\mathcal{L}_5$ to allow for all internal unknown forces to be determined. This set of simultaneous equations is expressed in matrix form as Equations (16) and (19) below.

The specific case of $\mathcal{L}_1$ needs to be given consideration before the full set of equations is presented. Figure 5 shows the free-body diagram for the shock strut as viewed perpendicular to the retraction plane (along the global X-axis). The force and moment equilibrium equations for $\mathcal{L}_1$ can be constructed in a similar manner to those for the sidestays and locklinks; however, the joint equilibrium equations between $\mathcal{L}_1$ and the adjoining links $\mathcal{L}_3$ and $\mathcal{L}_5$ require the application of the inverse T^{-1} of the transformation matrix T to express the sidestay and locklink local forces in the global coordinate system in which the shock strut is considered. The joint equilibrium equation for the sidestay-shock strut and locklink-shock strut joints (B and E) respectively, are given by

$$\begin{aligned}\mathcal{F}_{1;3} &= -T^{-1} F_{3;1}\,, \\ \mathcal{F}_{1;5} &= -T^{-1} F_{5;1}\,,\end{aligned} \tag{11}$$

where T^{-1} contains elements $t_{m,n}$ (where $m, n \in \{1, 2, 3\}$). Equation (11) can be expanded by multiplying out the right-hand side. Since the links are assumed to be rigid, only forces acting in the shock strut rotation plane influence the moment equilibrium of the link; therefore expressions for the X-components of the global forces ($\mathcal{F}^X_{1;3}$ and $\mathcal{F}^X_{1;5}$) can be neglected. Equation (12) describes the four internal structural forces shown in Figure 5:

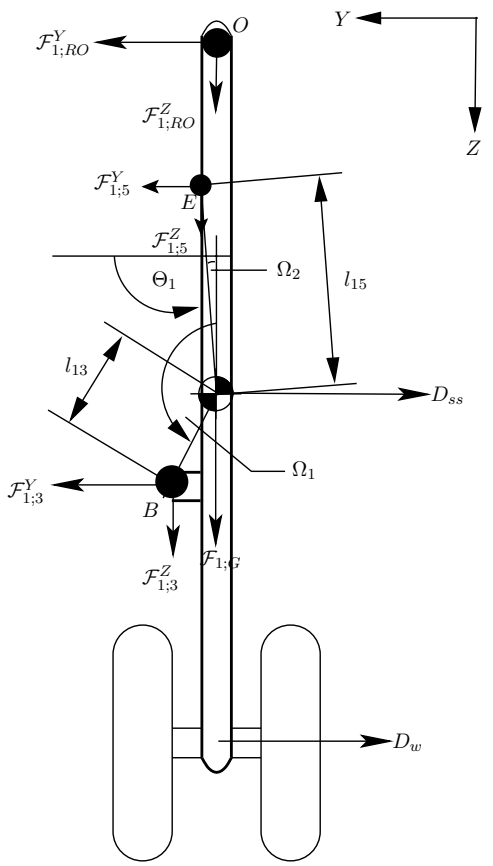

Fig. 5: Free-body diagram of the main strut $\mathcal{L}_1$ described in global co-ordinates.

$$\mathcal{F}^Y_{1;3} = -(t_{2,1}F^x_{3;1} + t_{2,2}F^y_{3;1} + t_{2,3}F^z_{3;1})\,, \tag{12a}$$

$$\mathcal{F}^Z_{1;3} = -(t_{3,1}F^x_{3;1} + t_{3,2}F^y_{3;1} + t_{3,3}F^z_{3;1})\,, \tag{12b}$$

$$\mathcal{F}^Y_{1;5} = -(t_{2,1}F^x_{5;1} + t_{2,2}F^y_{5;1} + t_{2,3}F^z_{5;1})\,, \tag{12c}$$

$$\mathcal{F}^Z_{1;5} = -(t_{3,1}F^x_{5;1} + t_{3,2}F^y_{5;1} + t_{3,3}F^z_{5;1})\,. \tag{12d}$$

The y and z components of $F_{3;1}$ and $F_{5;1}$ are described from the equilibrium equations of the sidestay $\mathcal{L}_3$ and locklink $\mathcal{L}_5$ respectively, but the out-of-plane components in the local x-direction ($F^x_{3;1}$ and $F^x_{5;1}$) require calculating. Because the mechanism, when cut anywhere, must still be in equilibrium, Figure 6 shows the free-body diagram used to obtain $F^x_{3;1}$ and $F^x_{5;1}$.

The x-components of the three unknowns in Figure 6, $F_{3;1}$, $F_{5;1}$ and $F_{2;RA}$, can be obtained by:

- Applying moment equilibrium about axis $\overline{OB}$;
- Resolving perpendicularly to the sidestay rotation plane (i.e. in the direction of $\hat{n}$);

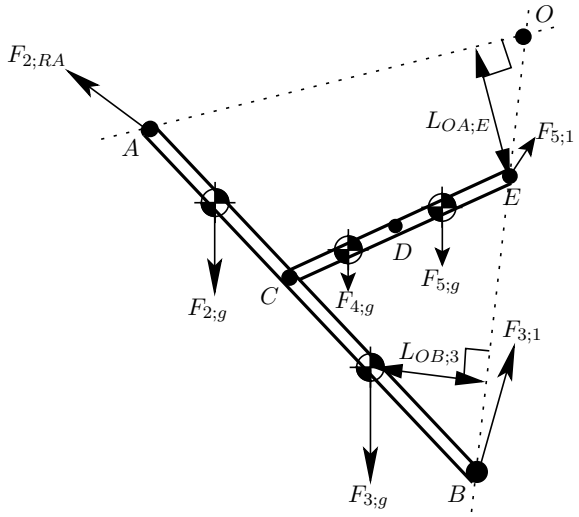

Fig. 6: Free-body diagram of the sidestay and locklinks expressed in local co-ordinates.

- Applying moment equilibrium about axis $\overline{OA}$.

The x-components of the forces shown in Figure 6 are assigned to act in a positive direction out of the page. Applying moment equilibrium about axis $\overline{OB}$ yields $F^x_{2;RA}$ directly as

$$F^x_{2;RA} = \tfrac{-1}{L_{OB;A}}(\, F^x_{2;g}L_{OB;2} + F^x_{3;g}L_{OB;3} + F^x_{4;g}L_{OB;4} + F^x_{5;g}L_{OB;5}). \tag{13}$$

Here, as before, $F^x_{2;RA}$ is the x-component of force $F_{2;RA}$. The generalised moment arm $L_{OB;*}$, is the shortest length from axis $\overline{OB}$ to point $*$. The example shown in Figure 6 depicts the moment arm $L_{OB;3}$ which is the moment arm of the lower sidestay's weight ($F_{3;g}$) about axis $\overline{OB}$. After obtaining $F^x_{2;RA}$, the following two expressions can be solved simultaneously to obtain $F^x_{3;1}$ and $F^x_{3;1}$:

$$F^x_{2;RA} + F^x_{2;g} + F^x_{3;g} + F^x_{4;g} + F^x_{5;g} + F^x_{3;1} + F^x_{5;1} = 0\,, \tag{14a}$$

$$F^x_{2;g}L_{OA;2} + F^x_{3;g}L_{OA;3} + F^x_{4;g}L_{OA;4} + F^x_{5;g}L_{OA;5} + F^x_{3;1}L_{OA;B} + F^x_{5;1}L_{OA;E} = 0\,. \tag{14b}$$

In Equation (14b) the generalised moment arm $L_{OA;*}$, is the shortest length from axis $\overline{OA}$ to point $*$. The example shown in Figure 6 depicts the moment arm $L_{OA;E}$ which is the moment arm of the internal force $F_{5;1}$ about axis $\overline{OA}$.

The moment equilibrium for the shock strut can now be expressed in terms of four unknown forces (the y and

z components of $F_{3;1}$ and $F_{5;1}$ — to be determined by solving all the internal force equations simultaneously) and two known forces ($F^x_{3;1}$ and $F^x_{5;1}$).

2.4 Matrix Formulation

With all internal force equilibrium equations constructed, the system of internal force equations can be written in matrix form as

$$A\overline{F} - \overline{B} = 0\,. \tag{15}$$

Here:

$$A = \begin{bmatrix}
-L_2 s\theta_2 & L_2 c\theta_2 & 0\ 0 & 0 & 0 & 0\ 0 & 0 & 0 & 0 & 0 & 0\ 0 & 0 & 0 & 0 & 0 & 0 \\
0 & 0 & 1\ 0 & 1 & 0 & 0\ 0 & 0 & 0 & 0 & 0 & 0\ 0 & 0 & 0 & 0 & 0 & 0 \\
0 & 0 & 0\ 1 & 0 & 1 & 0\ 0 & 0 & 0 & 0 & 0 & 0\ 0 & 0 & 0 & 0 & 0 & 0 \\
0 & 0 & 0\ 0 & -L_3 s\theta_3 & L_3 c\theta_3 & 0\ 0 & 0 & 0 & 0 & 0 & 0\ 0 & 0 & 0 & 0 & 0 & 0 \\
0 & 0 & 0\ 0 & 0 & 0 & 1\ 0 & 1 & 0 & 0 & 0 & 0\ 0 & 0 & 0 & 0 & 0 & 0 \\
0 & 0 & 0\ 0 & 0 & 0 & 0\ 1 & 0 & 1 & -1 & 0 & 0\ 0 & 0 & 0 & 0 & 0 & 0 \\
0 & 0 & 0\ 0 & 0 & 0 & 0\ 0 & L_4 s\theta_4 & -L_4 c\theta_4 & L_4 c\theta_4 & 0 & 0\ 0 & 0 & 0 & 0 & 0 & 0 \\
0 & 0 & 0\ 0 & 0 & 0 & 0\ 0 & 0 & 0 & 0 & 1 & 0\ 1 & 0 & 0 & 0 & 0 & 0 \\
0 & 0 & 0\ 0 & 0 & 0 & 0\ 0 & 0 & 0 & 0 & 0 & 1\ 0 & 1 & 0 & 0 & 0 & 0 \\
0 & 0 & 0\ 0 & 0 & 0 & 0\ 0 & 0 & 0 & 0 & 0 & 0\ -L_5 s\theta_5 & L_5 c\theta_5 & 0 & 0 & 0 & 0 \\
0 & 0 & 0\ 0 & 0 & 0 & 0\ 0 & 0 & 0 & 0 & 0 & 0\ 0 & 0 & C_1 & C_2 & C_3 & C_4 \\
1 & 0 & 1\ 0 & 0 & 0 & 1\ 0 & 0 & 0 & 0 & 0 & 0\ 0 & 0 & 0 & 0 & 0 & 0 \\
0 & 1 & 0\ 1 & 0 & 0 & 0\ 1 & 0 & 0 & 0 & 0 & 0\ 0 & 0 & 0 & 0 & 0 & 0 \\
0 & 0 & 0\ 0 & 0 & 0 & 0\ 0 & 1 & 0 & 0 & 1 & 0\ 0 & 0 & 0 & 0 & 0 & 0 \\
0 & 0 & 0\ 0 & 0 & 0 & 0\ 0 & 0 & 1 & 0 & 0 & 1\ 0 & 0 & 0 & 0 & 0 & 0 \\
0 & 0 & 0\ 0 & 0 & 0 & 0\ 0 & 0 & 0 & 0 & 0 & 0\ t_{2,2} & t_{2,3} & 0 & 0 & -1 & 0 \\
0 & 0 & 0\ 0 & 0 & 0 & 0\ 0 & 0 & 0 & 0 & 0 & 0\ t_{3,2} & t_{3,3} & 0 & 0 & 0 & -1 \\
0 & 0 & 0\ 0 & t_{2,2} & t_{2,3} & 0\ 0 & 0 & 0 & 0 & 0 & 0\ 0 & 0 & -1 & 0 & 0 & 0 \\
0 & 0 & 0\ 0 & t_{3,2} & t_{3,3} & 0\ 0 & 0 & 0 & 0 & 0 & 0\ 0 & 0 & 0 & -1 & 0 & 0
\end{bmatrix}, \tag{16}$$

where $s \equiv \sin$, $c \equiv \cos$ and

$$\begin{bmatrix} C_1 \\ C_2 \\ C_3 \\ C_4 \end{bmatrix} = \begin{bmatrix} \frac{L_1}{2}\sin\Theta_1 - l_{13}\sin(\Theta_1 + \Omega_1) \\ l_{13}\cos(\Theta_1 + \Omega_1) - \frac{L_1}{2}\cos\Theta_1 \\ \frac{L_1}{2}\sin\Theta_1 - l_{15}\sin(\Theta_1 - \Omega_2) \\ l_{15}\cos(\Theta_1 - \Omega_2) - \frac{L_1}{2}\cos\Theta_1 \end{bmatrix}, \tag{17}$$

$$\overline{F} = -\left[\, F^y_{2;3,4} F^z_{2;3,4} F^y_{3;2,4} F^z_{3;2,4} F^y_{3;1} F^z_{3;1} F^y_{4;2,3} F^z_{4;2,3} F^y_{4;5} F^z_{4;5} F_{unlock} F^y_{5;4} F^z_{5;4} F^y_{5;1} F^z_{5;1} \mathcal{F}^y_{1;3} \mathcal{F}^z_{1;3} \mathcal{F}^y_{1;5} \mathcal{F}^z_{1;5} \,\right]^T, \tag{18}$$

where F_{unlock} is an external force which represents the unlock actuator force on the landing gear mechanism, and

$$\overline{B} = - \begin{bmatrix} \frac{L_2}{2} m_2 g_z \cos\theta_2 - \frac{L_2}{2} m_2 g_y \sin\theta_2 \\ m_3 g_y \\ m_3 g_z \\ \frac{L_3}{2} m_3 g_z \cos\theta_3 - \frac{L_3}{2} m_3 g_y \sin\theta_3 \\ m_4 g_y \\ m_4 g_z \\ -\frac{L_4}{2} m_4 g_z \cos\theta_4 + \frac{L_4}{2} m_4 g_y \sin\theta_4 \\ m_5 g_y \\ m_5 g_z \\ \frac{L_5}{2} m_5 g_z \cos\theta_5 - \frac{L_5}{2} m_5 g_y \sin\theta_5 \\ \\ -(\frac{m_1}{2} G_z + m_{wheel}) L_3 \cos\Theta_1 \\ -F^z_{act}(l_{1act}\cos(\Theta_1 + \Omega_3)) \\ +F^y_{act}(l_{1act}\sin(\Theta_1 + \Omega_3)) - M_D + M \\ \\ 0 \\ 0 \\ 0 \\ 0 \\ -t_{2,1} F^x_{5;1} \\ -t_{3,1} F^x_{5;1} \\ -t_{2,1} F^x_{3;1} \\ -t_{3,1} F^x_{3;1} \end{bmatrix} . \quad (19)$$

Here M is the retraction actuator moment parameter, F_{act} is the actuator force parameter (both initially chosen to be zero to reflect the deployed MLG state) and M_D is the drag-induced moment (described below); length l_{1act} is the distance from the shock strut cg to the adjoining retraction actuator, and Ω_3 is the angle that the length l_{1act} makes with the shock strut centreline (in local co-ordinates).

One reason for formulating the landing gear force balance equations in matrix form is to ease calculation of the initial conditions which, in general, can be obtained by computing $A^{-1}\overline{B}$. In some initialisation cases, where the locklinks are horizontal and the main fitting is vertically perpendicular to the locklinks, A becomes singular so cannot be inverted to find an initial point. This was not the case for the MLG considered here and, in general, this issue of a singular matrix A can be avoided by starting from a partially retracted configuration.

2.5 Drag-Induced Moment

To ensure the model remains as general as possible, an analytical expression for the drag-induced moment M_D in Equation 19 is derived. For simplification purposes, it is assumed that there are two main contributing elements to the overall drag — the shock strut and wheel assembly — and that the drag of these elements acts from the geometric centres. The drag moment M_D can therefore be expressed in terms of two drag forces:

$$M_D = L_3(\frac{1}{2} D_{ss} + D_w) . \quad (20)$$

The drag forces are derived from the standard expression for aerodynamic drag on a body in incompressible, steady flow:

$$D = \frac{1}{2}\rho V^2 S C_D . \quad (21)$$

Here:

- D is the component of drag force in the global (Y,Z)-plane acting upon the body;
- ρ is the air density (sea level conditions assumed, where ρ can be taken as $1.225 \frac{kg}{m^3}$);
- V is the air velocity component contributing to drag on the body of interest;
- S is the 'wetted area' of the body, i.e. the maximum cross-sectional area of the body that the flow moves over;
- C_D is the drag coefficient of the body.

The drag force on the landing gear is assumed to consist of two separate parts: the drag on the shock strut and the drag on the wheels. The drag coefficients for these two parts are calculated by approximating the shock strut as a cylinder and the wheels as disks with a depth less than their diameter, and obtaining values for the drag coefficients of these shapes from the literature. The wetted areas for these two shapes are calculated using an estimated average radius for the shock strut and the radius of each wheel. For the purposes of this analysis, the air velocity of interest is the velocity component which acts in the shock strut rotation plane (i.e. in the (Y, Z) plane). With these assumptions, the drag force on the shock strut (D_{ss}) and on each wheel (D_w) becomes:

$$D_{ss} = \frac{1}{2}\rho(U_\infty \cos(\alpha - \theta_1 + \frac{\pi}{2})^2 (L_1 d) C_{Dss} , \quad (22a)$$

$$D_w = \frac{1}{2}\rho(U_\infty \cos(\alpha - \theta_1 + \frac{\pi}{2})^2 (\pi r^2) C_{Dw} . \quad (22b)$$

Here:

Table 1: Values of the parameters used in this case study.

Parameter	Value	Parameter	Value	Parameter	Value
L_1	2.90 m	ω_2	1.90°	C_{Dss}	0.600
L_2	0.777 m	Ω_1	142°	C_{Dw}	1.17
L_3	1.17 m	Ω_2	1.77°	m_1	2300 kg
L_4	0.419 m	α	0°	m_2	200 kg
L_5	0.628 m	U_∞	0 m/s	m_3	110 kg
l_{13}	0.270 m	ρ	1.225 $\frac{kg}{m^3}$	m_4	7 kg
l_{15}	1.12 m	d	0.5 m	m_5	7 kg
ω_1	136°	r	0.4 m	m_{wheel}	400 kg
a	0.290 m	b	0.290 m	ψ_d	6°

- U_∞ is the magnitude of the air velocity in the (Y, Z) plane;
- α is the angle between the airflow direction and the global Y-axis (set to zero in this paper);
- d is the diameter of the main fitting;
- C_{Dss} is the drag coefficient of the main fitting of the landing gear
- r is the radius of the landing gear wheel;
- C_{Dw} is the drag coefficient of the wheel of the landing gear

To calculate the resulting moment, the drag forces were assumed to act at the c/g of their respective bodies, so:

$$\begin{aligned} M_D &= L_3(\tfrac{1}{2}D_{ss} + D_w) \\ &= \tfrac{1}{4}\rho(U_\infty \cos(\alpha - \theta_1 + \tfrac{\pi}{2})^2 \\ &\quad \times (d(L_3^2)C_{Dss} + 2\pi r^2 C_{Dw})\,. \end{aligned} \tag{23}$$

3 Bifurcation Analysis of Actuator Placement

This case study is presented to demonstrate the potential benefits of using numerical continuation methods in the design phase of an aircraft. The actuator position has a direct influence on several key design objectives, including the peak actuator force and the retraction efficiency. The results presented here are for a MLG retracting perpendicularly to the onset flow — as such, the air velocity, and hence the drag-induced moment M_D in the model, is set to zero throughout. This corresponds to the case of an aircraft flying in a straight line without experiencing any sideslip motion, which is a realistic case to consider for the purposes of this investigation.

Table 1 provides details of the initial parameter values used within the model during this case study. The values were chosen to be representative of the MLG of a generic medium-sized passenger aircraft's main landing gear, such as a Boeing 737 or an Airbus A320. It should be noted though that these are only defined as parameters by convention; the model flexibility enables any of these parameters to be treated in the numerical continuation as a model state provided an appropriate number of other variables are fixed, however for the purpose of this case study these parameter values remain fixed.

3.1 Actuator Parameterisation

Figure 7 shows how the actuator position is parameterised within the model. Three parameters are used to describe the actuator position: length a denotes the vertical distance between the shock strut rotation point and the actuator attachment point on the aircraft body; length b is the distance between the shock strut rotation point and the actuator attachment point on the shock strut; and angle ψ_d is the angle made in the deployed position between the actuator and the shock strut centreline. It should be noted that, whilst it would be possible to parameterise the actuator position in terms of three length parameters (a, b and $c = (a + b)\tan\psi$) rather than two lengths and one angle, the three length parameters would not be independent, and therefore distinguishing between parameter effects would be more difficult.

The actuator is positioned in the plane that the shock strut retracts in, as any out of plane actuator components would not contribute to retracting the landing gear. The actuator is also assumed to be attached to the shock strut centreline, something which is not necessarily the case for all real landing gears. The parameter a is fixed in the following results presented in this paper, and chosen to be equal to 10% of the shock-strut length L_1.

3.2 Influence of the Actuator Angle on Required Force

Figure 8(a) shows the curve of equilibrium solutions throughout the retraction cycle in terms of the actuator force F and retraction angle Θ_1, for parameters

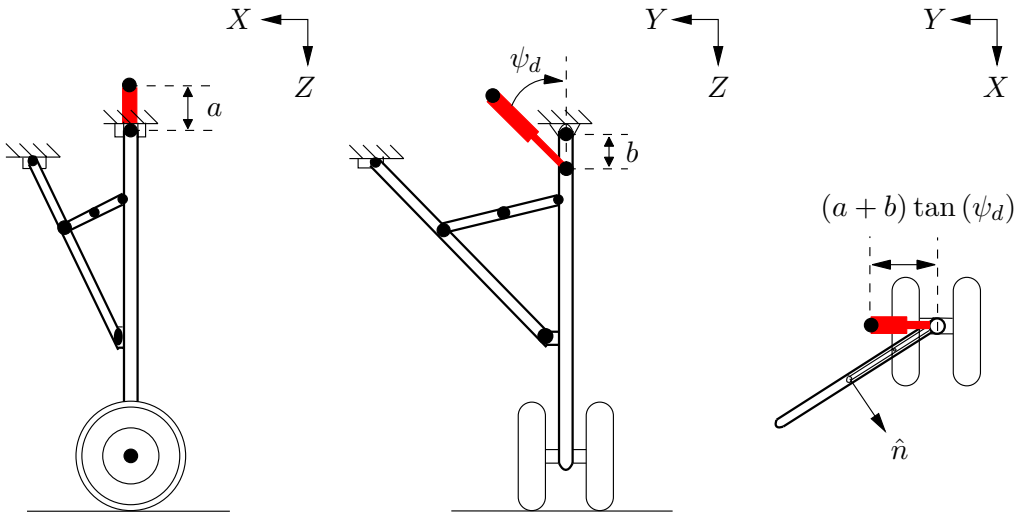

Fig. 7: Actuator parameterisation diagram.

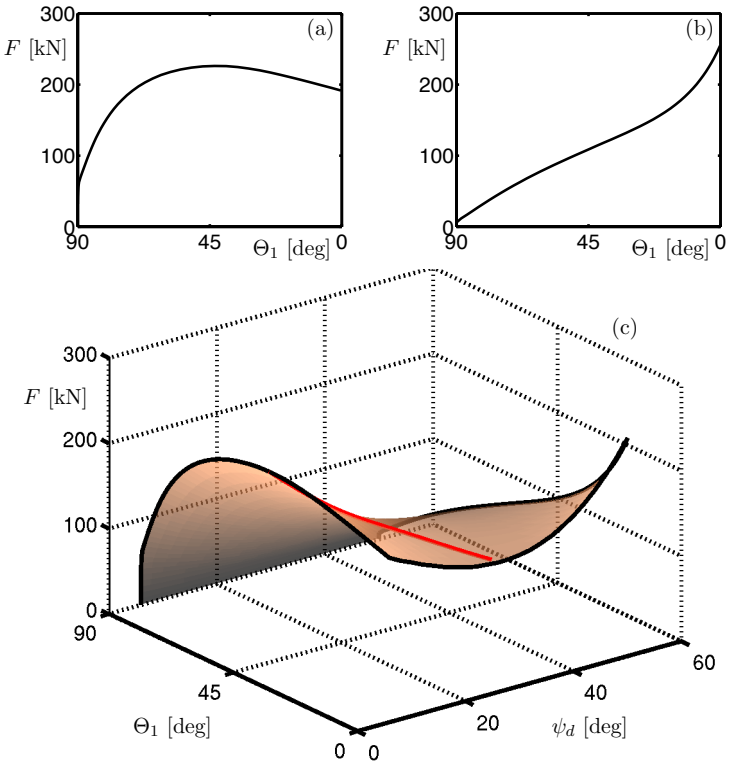

Fig. 8: Retraction/extension equilibria for $a = b = 10\%L_1$ shown in terms of actuator force F as a function of retraction angle Θ_1 for actuator angle $\psi_d = 6°$ (a) and $\psi_d = 50°$ (b). Panel (c) shows a surface of equilibria plotted in terms of F as a function of Θ_1 and ψ_d between 6° and 50°. The red curve denotes the local maxima of F.

$a = b = 0.29m$, i.e. 10% of shock strut length L_1, and an actuator moment angle of $\psi_d = 6°$. The landing gear starts in the deployed position with a retraction angle of $\Theta_1 = 90°$. As the gear retracts, Θ_1 decreases until the gear reaches the fully retracted position at $\Theta_1 = 0°$. The plot in Figure 8(a) shows the equilibrium information in terms of the actuator force F that is required to hold the landing gear in static equilibrium at a given retraction angle Θ_1. To obtain smooth motion in a real retraction or extension of the landing gear, the force variation would need to approximate this equilibrium curve.

The initially steep gradient is a result of the mechanism geometry; internal forces from the sidestay/locklink plane are transmitted into the main fitting at the sidestay and locklink attachment points. The moments created by these internal forces resist the initial motion of the main fitting, until the moment induced by the actuator overcomes the opposing moment of the sidestay and locklink forces. If the landing gear mechanism was locked, the actuator moment required to overcome the internal moments and begin the retraction cycle would be very large (practically infinite). To enable the gear to retract, an unlock actuator is used to partially unlock the locklinks before the retraction actuator retracts the gear.

Beyond the initial steep gradient, the actuator force required to hold the landing gear in equilibrium continues to increase as the landing gear retracts. This is because the out-of-plane gravitational forces acting on the sidestays and locklinks increase more than the actuator force projection working to retract the landing

gear. Beyond the local maximum force point, the landing gear requires less force from the actuator to hold the system in equilibrium as the retraction angle decreases: namely, beyond the local maximum, the out-of-plane gravitational force increase during retraction is overcome by the increased actuator force projection acting to retract the landing gear.

The implication of this decreasing equilibrium force is that the gear needs to be slowed down before it reaches the retracted position. For a constant landing gear actuator force value higher than the maximum equilibrium force, the landing gear will move upwards into the wing. In the absence of any actuator control, the landing gear will slam into the aircraft. To prevent this from happening, actuators used in service contain a damping element that works to slow down the actuator retraction rate, in turn slowing the gear down so that it comes to rest without impacting the wing box.

Figure 8(b) shows an equivalent curve of equilibrium solutions for an actuator moment angle of $\psi_d = 50°$. The curve is qualitatively different from the case of $\psi_d = 6°$: the initial gradient is quite shallow and, as the landing gear retracts, the gradient of this curve increases. The reason for the relatively shallow initial gradient is that the retraction actuator has a much larger component acting to retract the landing gear when $\psi_d = 50°$, so significantly less force is required to create the required retraction moment. Along the equilibrium curve, there is now no local maximum force; instead, the maximum actuator force for $\psi_d = 50°$ is the force required to hold the landing gear in the retracted state. The value of this maximum is slightly higher than the maximum force obtained for $\psi_d = 6°$.

Figure 8(c) graphically represents how the retraction equilibrium curve changes with different values of ψ_d between the two extreme cases shown in Figure 8(a) and (b). The surface of equilibria is bounded by a black curve for clarity, whilst the red curve on the surface is the locus of local maxima. The local maxima curve indicates actuator configurations which have a maximum force that occurs before the gear is fully retracted. Retraction cycles with a local maximum force are qualitatively similar to the case shown in Figure 8(a). For values of ψ_d where no local maximum is present in the retraction cycle, the maximum force occurs at the end of the retraction cycle and the retraction response is qualitatively similar to the case shown in Figure 8(b). It can therefore be seen from Figure 8(c) that the lowest peak actuator force is achieved for the actuator angle $\psi_d = 28°$, which is the value where the locus of local maxima disappears.

3.3 Actuator Length Requirements

In a real MLG, physical constraints will limit the positioning of the landing gear actuator. One of these constraints is the change in actuator length between the deployed position (where the actuator is extended) and the retracted position (where the actuator is contracted).

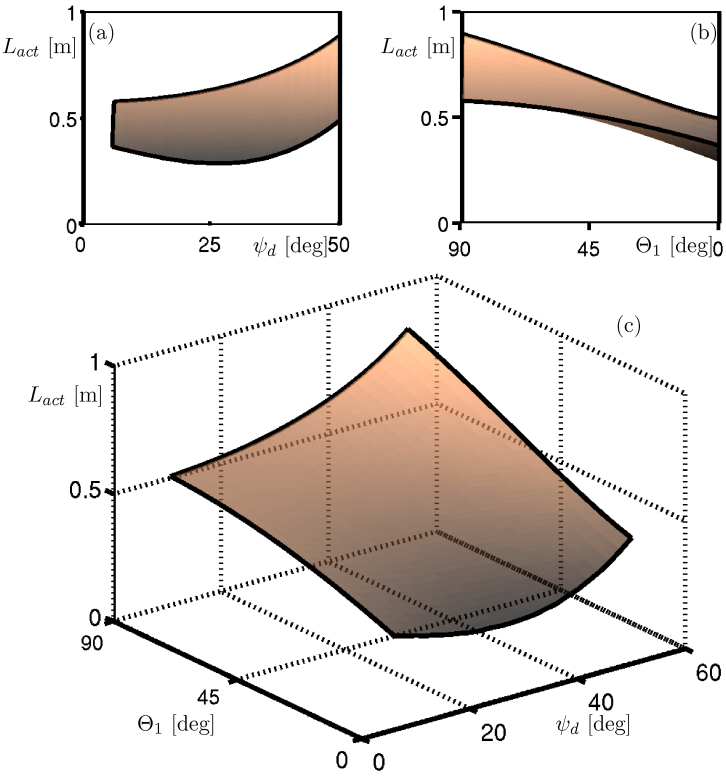

Fig. 9: Dependence of actuator length L_{act} on retraction angle Θ_1 and actuator angle ψ_d for a moment arm length of $b = 10\%L_1$. Panels (a) and (b) show projections onto the (L_{act}, Θ_1)-plane and (L_{act}, ψ_d)-plane, respectively, of the surface in panel (c).

Figure 9 shows how the actuator length depends on the retraction angle Θ_1 and the actuator angle ψ_d when the gear is in equilibrium. The equilibrium surface in Figure 9(c) is simply a different projection of the same equilibria shown in Figure 8(c); no new calculations were needed. The (L_{act}, Θ_1)-projection in Figure 9(b) shows that the maximum actuator length (which occurs in the deployed position) increases as the actuator angle is increased from 6° to 50°. A result that is slightly less obvious is the change in minimum actuator length (which occurs in the retracted position). The lower bound on the surface, shown in Figure 9(a), forms

a somewhat parabolic edge; the actuator length initially decreases as the actuator angle is increased before a minimum retracted actuator length occurs at $\psi_d = 30°$. This minimum length occurs when the horizontal distance between the actuator-airframe attachment point and the shock strut attachment point ($(a+b)\tan\psi_d$ as in Figure 7) equals the actuator moment arm b. For the case considered here where $a = b = 10\%L_1$, the minimum actuator length occurs in the retracted position when $\tan\psi_d = 0.5$, i.e. when $\psi_d = 30°$.

3.4 Actuator Efficiency Dependency on Actuator Angle

The efficiency $\mathcal{E}$ of the landing gear actuator is given by the ratio of the area under the curve of actuator force F as a function of actuator length L_{act} (area B in Figure 10(a) and (b)) to the area of the rectangle which bounds that curve (area A in Figure 10(a) and (b)) [3]. The efficiencies for the two cases shown in Figures 10(a) and (b) are 92% and 43% respectively. As before, when considering the retraction efficiency as the comparative measure, the case when $\psi_d = 6°$ would be a better choice than using $\psi_d = 50°$. The response shown in Figure 10(b) is of a type referred to by Conway [1] as a "bad retraction diagram", compared to the "typical retraction curve" of the response shown in Figure 10(a).

Figure 10(c) shows the equilibrium surface in (ψ_d, L_{act}, F)-space. As before, the edges of the surface are highlighted by black curves and the red curve is the locus of local maxima. The shadow on the bottom of the figure shows the top-down projection of the surface (the same view shown previously in Figure 9(a)). This figure depicts graphically three conflicting design drivers: the peak actuator force, to be minimised; the change in actuator length, to be minimised; and the actuator efficiency, to be maximised.

Figure 11 presents the three conflicting design drivers observable in Figure 10(c) in a more convenient manner. Figure 11(a) shows that the change in actuator length δL_{act} increases approximately linearly with ψ_d until about $\psi_d = 30°$, when the gradient decreases until the maximum point on the graph is reached. As the design driver would be to minimise δL_{act}, a small actuator angle would be most desirable from this perspective. A small value for ψ_d would also be desirable when considering the efficiency variation in Figure 11(b). This plot shows that as the actuator angle increases, the efficiency decreases. As a minimal δL_{act} would generally be most desirable from a design perspective, there would be no conflict in meeting both efficiency and length change design objectives.

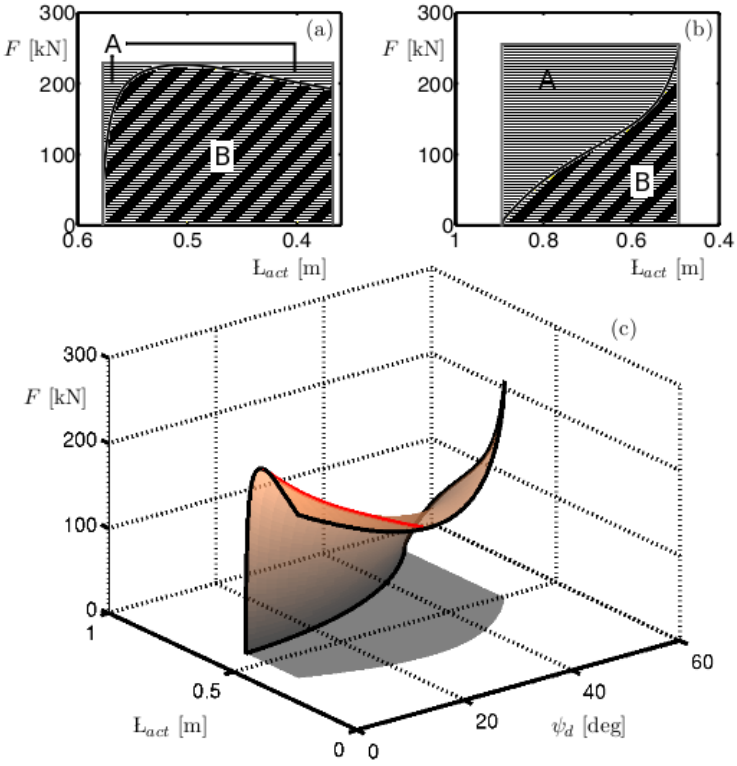

Fig. 10: Retraction/extension equilibria for $a = b = 10\%$ shock strut length in terms of actuator force F, actuator length L_{act} and actuator angle ψ_d, with ψ_d equal to (a) 6°, (b) 50° and (c) between 6° and 50°. The red curve in (c) denotes a fold bifurcation.

Figure 11(c) shows that the minimum peak actuator force F_{act} occurs above the lowest value of ψ_d considered – far from the actuator angle that would minimise δL_{act} and maximise efficiency. It would therefore be necessary to consider further factors (such as the influence of these measures on actuator weight, operating cost, manufacturing cost, etc.) to make an informed design decision regarding actuator placement within this example landing gear system.

It should be noted that, whilst it would be possible to use some form of optimising routine to attempt to find an 'optimum' actuator position, the objective function to be optimised heavily influences the outcome. For preliminary design work, the ability to accurately visualise how different parameters affect a variety of design objectives allows a global picture of the underlying system behaviour to be built. Clear information about the implications of design decisions, as provided here, may aid the formulation of appropriate design criteria at an early stage.

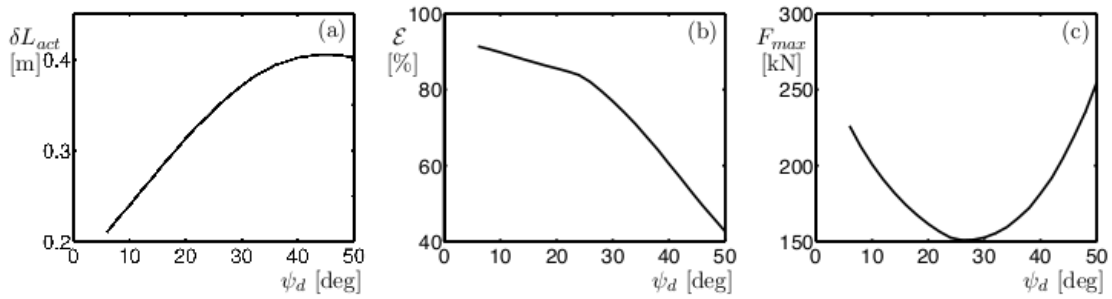

Fig. 11: Comparison of actuator length δL_{act} (a); actuator efficiency $\mathcal{E}$ (b), and peak actuator force F_{max} (c) with increasing deployed actuator angle ψ_d.

3.5 Influence of Increasing Moment Arm

The effect of increasing the actuator moment arm b is presented in Figure 12, where the corresponding changes to the surface of equilibria are shown. The case examined up to this point is that in Figure 12(a) for $b = 10\%L_1$. Increasing the moment arm to $b = 15\%L_1$ reduces the peak actuator force required for a given actuator angle. The overall effect is that the equilibrium surface is now lower in the projections shown and, hence, for a given initial actuator angle, increasing b would decrease the actuator force required to maintain the gear in equilibrium at any given point throughout the retraction cycle. This is an intuitive result because the parameter b is the effective actuator moment arm. Further increases in b cause the peak actuator force to continue to decrease, although the amount of this force reduction appears to diminish as b is increased through Figures 12(c) to (f).

A less intuitive result is observed when considering how the locus of local maxima changes as b increases. From Figure 12(a) to (b), the curve of maxima moves such that its endpoint at $\Theta_1 = 0$ disappears at a higher value of ψ_d. This endpoint still coincides with the minimum peak actuator force point, so the equilibrium surface for $b = 15\%L_1$ is qualitatively similar to that for $b = 10\%L_1$. As b is increased further to $b = 20\%L_1$, a qualitative change in the surface is observed. The local maxima curve moves such that its endpoint at $\Theta_1 = 0$ no longer coincides with the minimum peak actuator force; see Figure 12(c). A further increase in the actuator moment arm from $b = 20\%L_1$ to $b = 25\%L_1$ causes the disappearance of the local maxima curve from the ψ_d range considered; see Figure 12(d) – (f).

Figure 13 plots the efficiencies, change in actuator lengths and peak forces for the six cases of actuator moment arm b in Figure 12. As the change in actuator length is a purely geometric property of the system, increasing b simply scales δL_{act}. Hence, in Figure 13(a), the shape of the curves remain unchanged qualitatively. This information enables physical bounds to be imposed on the actuator length change during the retraction cycle; since the actuator must fit in a confined space, the maximum actuator length is required to be kept within any space limits.

Figure 13(b) shows efficiency curves, which change significantly as b is increased. There is a qualitative change that sees a second efficiency peak form for values of $\psi_d \approx 37\%$ when b reaches $25\%L_1$. The reason for this qualitative change relates to several observable changes in the equilibrium surfaces of Figure 12 along with the variation in maximum force depicted in Figure 13(c). These changes are explained by considering the two extreme cases for b (i.e. $b = 10\%L_1$ and $b = 35\%L_1$).

When $b = 10\%L_1$, the change in peak actuator force with actuator angle is relatively small, decreasing from 230 kN to its minimum of 180kN as ψ_d increases from 6° to 27° Figure 13(c). Within this actuator angle range, the peak force occurs at the local maxima indicated in Figure 12(a). In these cases, the load-displacement curve has a sharp gradient initially which gradually decreases to the maximum force value in a manner as shown in Figure 10(a), which is an efficient way to retract the gear. Once the local maxima have disappeared, the peak force increases as ψ_d is increased, and the retraction cycle begins to look more like the response shown in Figure 10(b), with a shallow gradient initially that increases as the gear retracts. This type of response is less efficient, as depicted by the efficiency curve for $b = 35\%$ in Figure 13(b). It is interesting to note the abrupt change in gradient observed in the (ψ_d, $\mathcal{E}$)-curve for $b = 10\%L_1$ when the actuator angle is increased beyond the angle of minimum actuator force (approximately $\psi_d = 25°$). The change in gradient means that, whilst low actuator angles for $b = 10\%L_1$ provide an efficient retraction response, there is a range

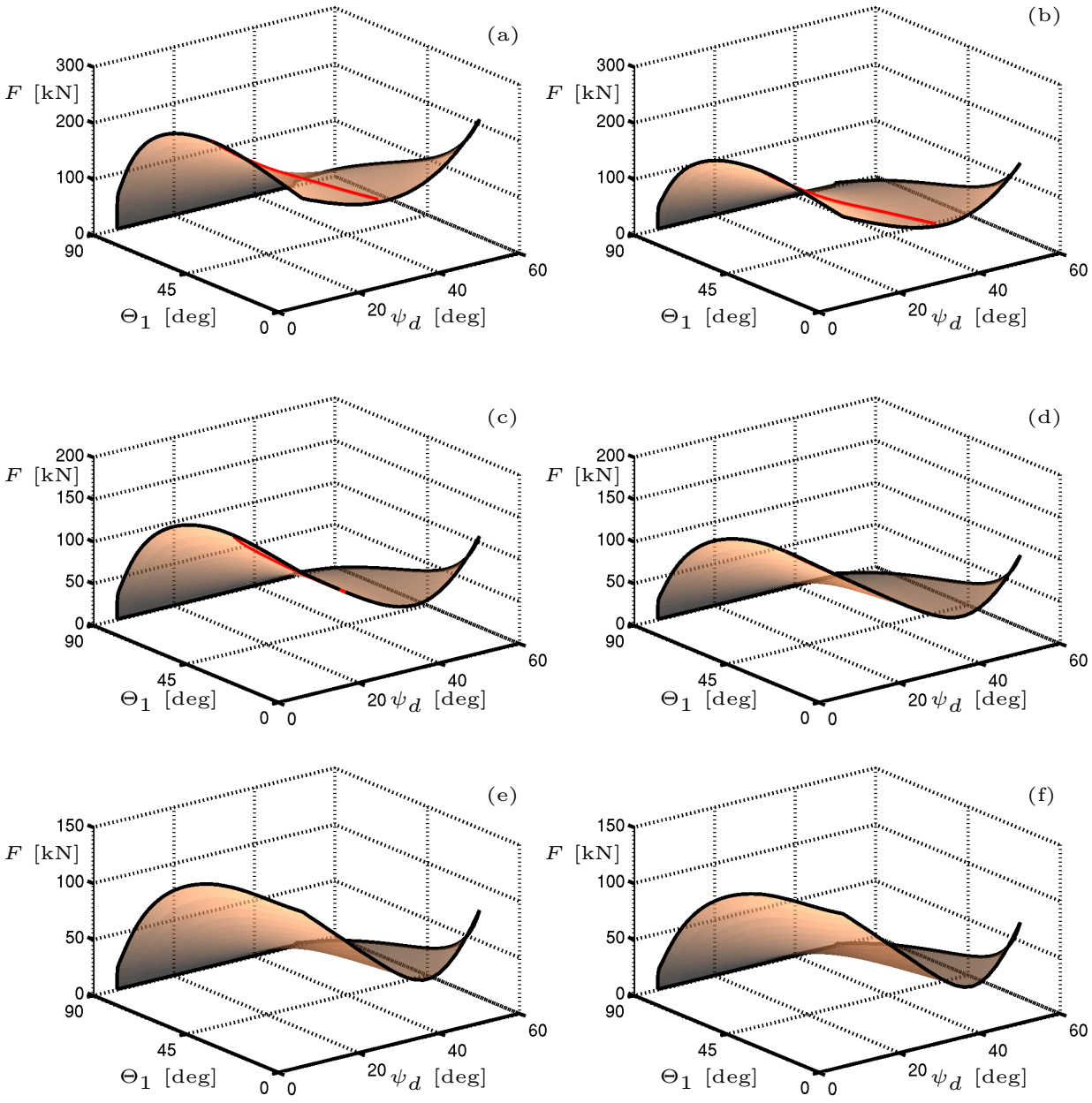

Fig. 12: Surface of retraction/extension equilibria for different parameter values with b ranging from (a) 10% to (f) 35% of the shock strut length in steps of 5% for intermediate panels (b)-(e)

of actuator angles over which $b = 10\%L_1$ is actually the least efficient of all the six actuator configurations investigated. This shows just how sensitive the actuator efficiency can be to changes in actuator placement, and highlights the importance of design tools that can capture counter-intuitive behaviour in a succinct manner.

When b has been increased to 35%, no local maxima are present on the equilibrium surface of Figure 12(f) and the percentage change in peak force over the actuator angle range considered has increased significantly. Figure 13(c) shows that the maximum peak force when $b = 35\%L_1$ is 140kN, and occurs when $\psi_d = 6°$. As ψ_d increases, this peak force value decreases linearly until the minimum peak force of 40kN is reached at $\psi_d = 38°$. Over this range of retraction angles (i.e. $6° \leq \psi_d \leq 38°$) the relation between L_{act} and ψ_d shown in Figure 13(a) is also linear, so the resultant efficiency variation with

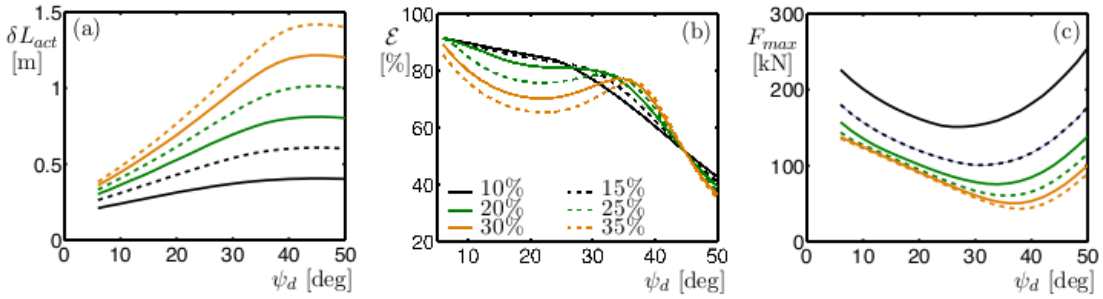

Fig. 13: Effect of increasing actuator moment arm b on: (a) actuator efficiency $\mathcal{E}$; (b) change in actuator length δL_{act}; (c) peak actuator force F_{max}, as functions of actuator angle ψ_d

increasing actuator angle can be primarily attributed to the change in retraction profile.

3.6 Purely Geometric Analysis of Actuator Position

There are two factors that contribute to the retraction behaviour as analysed with the numerical continuation approach. The first is the internal force distribution: as the gear retracts, the forces acting between the links change as a result of changing link angles and in-pane weight. This internal force distribution is complex, and the numerical continuation approach is probably the simplest method for determining these internal forces. The second factor contributing to the observed retraction behaviour is the geometry of the actuation. As the MLG retracts, the actuator force projection varies. By creating an analytical expression for this force projection variation, the continuation results can be qualitatively validated and some of the observed behaviour explained in terms of the actuation geometry.

The results of the continuation study of the full MLG model are now compared with those of a simplified, purely geometric evaluation of actuator placement, by initially considering how the actuator force component perpendicular to the main strut varies as a function of the deployment angle Θ_1. Figure 14 depicts the purely geometric scenario considered. The actuator is parameterised in terms of the three parameters a, b and ψ_d, as used in the continuation analysis. Figure 14(a) shows the geometric situation for a deployed landing gear, where the angle between the actuator and the shock strut $\psi = \psi_d$, and the deployment angle $\Theta_1 = 90°$. Figure 14(b) depicts a partially-retracted state, and Figure 14(c) shows the fully retracted case when $\Theta_1 = 0°$. Since the component of this actuator force F_g acting to retract the main fitting is given by $F_g \sin\psi$, an expression for $\sin\psi$ will show how the geometry affects the retraction force. Using sine and cosine rules yields the following expressions in terms of the geometric elements depicted:

$$\frac{(a^2+c^2)^{1/2}}{\sin\psi} = \frac{L}{\sin(\Theta_1 + \tan^{-1}(a/c))}\,, \tag{24}$$

$$L^2 = b^2+a^2+c^2-2b(a^2+c^2)^{1/2}\cos(\Theta_1+\tan^{-1}(a/c)))\,, \tag{25}$$

where $c = (a+b)\tan\psi_d$ is used to simplify the above expressions. Substituting the expression for L in Equation (25) into Equation (24) gives the expression for $\sin\psi$ as a function of Θ_1 in terms of the parameters a, b and ψ_d as:

$$\sin\psi = \frac{(a^2+c^2)^{1/2}\sin(\Theta_1+\tan^{-1}(a/c))}{\sqrt{b^2+a^2+c^2-2b(a^2+c^2)^{1/2}\cos(\Theta_1+\tan^{-1}(a/c)))}}\,. \tag{26}$$

As well as the variation in force projection, it was reasoned that, as the landing gear retracts, the mass component acting against the retraction (i.e. perpendicular to the sidestay rotation plane) increases, and that this increase is described approximately by the cosine of the retraction angle Θ_1, i.e. $M \propto \cos\Theta_1$.

Figure 15 compares M as a function of Θ_1, as obtained from numerical continuation, with the cosine approximation for this same relation. For comparative purposes, the cosine response has been scaled by the maximum retraction moment M_{max}, obtained from the continuation results. By assuming that this retraction moment is created by the retraction actuator, the retraction moment can be approximated by $M = F_g b \sin\psi$, and the geometric retraction force F_g can therefore be represented by:

$$\begin{aligned} F_g &= \tfrac{\cos\Theta_1}{b\sin\psi} \\ &= \cos\Theta_1 \\ &\times \frac{\sqrt{b^2+a^2+c^2-2b(a^2+c^2)^{1/2}\cos(\Theta_1+\tan^{-1}(a/c)))}}{b(a^2+c^2)^{1/2}\sin(\Theta_1+\tan^{-1}(a/c))}\,. \end{aligned} \tag{27}$$

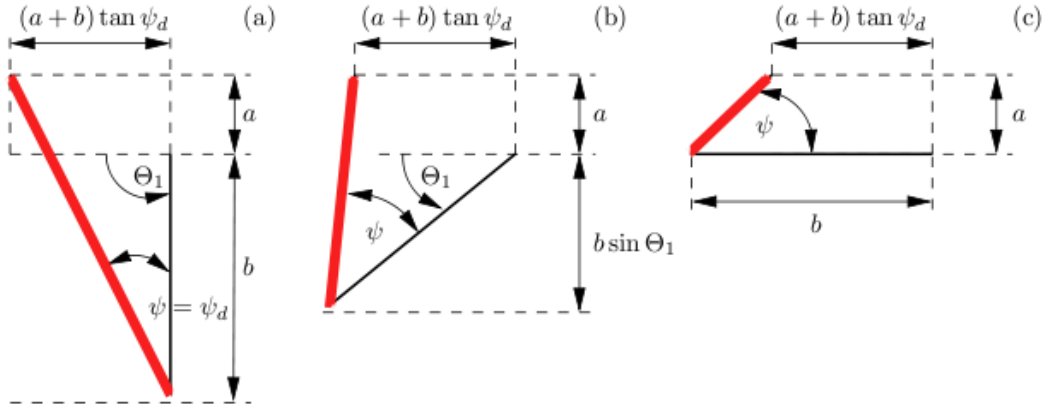

Fig. 14: Geometry of landing gear actuator (thick line of variable length L) and shock strut (thin solid line of fixed length b) shown in the deployed position ($\psi = \psi_d$) in (a), a partially-retracted state in (b), and the fully retracted position in (c).

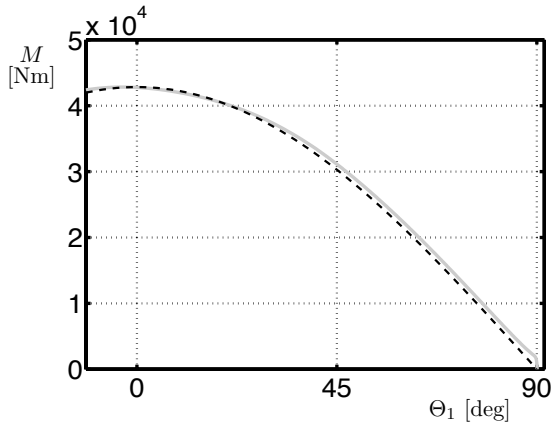

Fig. 15: A comparison of the retraction moment M as a function of retraction angle Θ_1 as obtained from the continuation analysis (solid grey curve) with $M_{max}\cos\Theta_1$ (dashed black curve).

This expression comprises the purely geometric effect of the changing actuator force projection $\sin\psi$ given by Equation (26), along with a significantly simplified representation of the effect of the landing gear mass. In particular, Equation (27) does to include the (geometrically unknown) mass, meaning that F_g is effectively non-dimensionalised. Furthermore, the analytical formula still requires numerical analysis tools to evaluate and interpret the equation.

Figure 16 plots F_g from Equation (27) as a function of Θ_1 in panels (a) and (b). It should be noted that no units have been assigned to the actuator force variable F_g since it is in units of landing gear weight. With the inclusion of the moment variation, it can be seen that Equation (27) captures the variation in equilibrium solutions shown in the continuation results. Furthermore, the surface produced from the geometric analysis in Figure 16(c) also reflects how the loci of equillibria change as the actuator moment arm b is varied. This suggests that the relatively simple Equation (27) captures much of the essence of the behaviour seen in the continuation analysis results. In this case, it provides a qualitative validation of the continuation results that highlights the effects of actuator geometry on the retraction cycle properties.

There are, however, some differences between the geometric force F_g and the equivalent numerical continuation analysis result for the retraction force F from Figure 8. For F_g, the shape of the response obtained for low ψ_d values is flatter[2], whilst for high values of ψ_d the geometric analysis produces a response with a more pronounced force peak at the end of the retraction cycle. The reasons for these differences are attributed to the way the geometric analysis accounts for the rest of the landing gear structure. The assumption that the weight moment opposing the retraction motion varies in a cosine manner is approximately true but not exact. Figure 15, where the moment required to retract the MLG (in grey) is plotted alongside $M_{max}\cos\Theta_1$, shows that the actual moment variation is not exactly a cosine; in particular, the peak occurs beyond the fully retracted position (i.e. $\Theta_1 < 0°$). Moreover, other aspects of the force balance in the MLG are also not modelled geometrically.

[2] i.e. the gradient either side of the local maximum point remains quite shallow for a wide range of retraction angle values

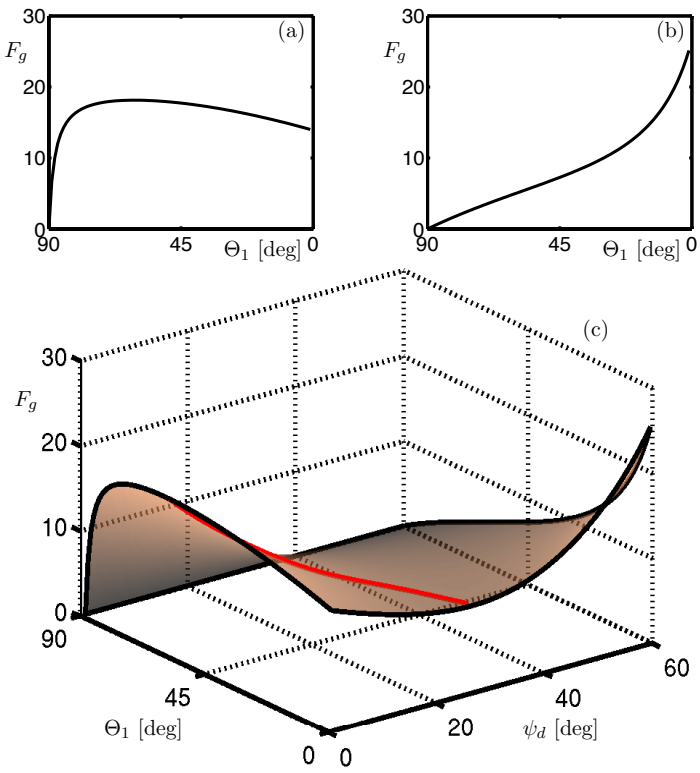

Fig. 16: Variation of theoretical actuator force F during the retraction cycle for the case when $a = b = 10\%L_1$ with deployed actuator angles of $\psi_d = 1°$ in (a), $\psi_d = 60°$ in (b), and between 1° and 60° in (c).

4 Concluding Remarks

It has been shown how a three-dimensional main landing gear retraction mechanism can be modelled as a set of fully parameterised steady-state constraint equations. This modelling approach is relatively simple yet flexible, and ideally suited for the use of numerical methods from bifurcation theory. In particular, it enables different landing gear configurations to be investigated with relative ease, saving modelling time by avoiding the need to make major model adaptations for a new gear configuration. The numerical continuation approach takes full advantage of this flexible formulation, allowing any model parameter of interest to be varied continuously. This is an advantage over traditional multibody dynamic simulations that are confined to running individual simulations for fixed values of system parameters.

The modelling and analysis approach was demonstrated with an investigation of MLG actuator placement from a design perspective. Several design parameters associated with the landing gear actuator were changed to investigate the resulting change in the retraction cycle. The numerical continuation approach allowed for convenient representation of equilibrium surfaces as functions of two design parameters: the model formulation complemented this by providing values for all states within the MLG mechanism directly, without needing to post-process the data to determine geometric dependencies of one model state of interest as a function of another. Increasing the actuator angle was shown to initially reduce the peak actuator force requirement, but there is a trade-off as the efficiency of the retraction cycle decreases over this same range. As well as providing information regarding retraction efficiency and peak actuator force, the model provided actuator length details from the same continuation data. It was suggested that this could be used to provide bounds to the design space when positioning the actuator based on space constraints within the airframe.

The numerical continuation approach was compared to a purely geometric model of actuator force projection. This highly simplified model qualitatively supported the findings from the numerical continuation analysis, and was useful for providing some insight into the underlying generic mechanisms. The purely geometric model however, does not consider the internal force balance and was found to be unable to provide qualitatively reliable results, thus strengthening the case for performing a continuation analysis of the full MLG equations.

With the increasing use of composite materials in primary structural elements of the next generation civil aircraft, future landing gear designs may require novel ways of reducing the point loads transferred into a carbon fibre wing box structure. One method of achieving this is to use a dual sidestay landing gear to redistribute the loads over multiple attachment points on the aircraft. The modelling approach presented here can be extended to a dual sidestay landing gear, resulting in 36 geometric constraints and 36 internal force constraints. The flexible approach offered by formulating the dual sidestay mechanism as a set of steady-state constraint equations, would enable design parameters, such as the angle between the two sidestays or the mass of a link, to be used as a continuation parameter in an investigation of the retraction cycle — something not easily achievable with conventional dynamic simulation methods.

References

1. Conway, H.G., *Landing Gear Design*, pp 1–4. Chapman and Hall, London, 1958.
2. Knowles, J.A.C., Krauskopf, B., Lowenberg, M.H., *Numerical Continuation Applied to Landing Gear Mechanism*

Analysis, AIAA Journal of Aircraft, Vol. 49, No. 8, July – August 2011.
3. Currey, N.S., *Aircraft Landing Gear Design: Principles and Practices*, pp 152–172. AIAA, Washington D.C, 1988.
4. Strogatz, S., *Nonlinear dynamics and chaos*, Springer, 2000.
5. Guckenheimer, J. and Holmes, P., *Nonlinear Oscillations, Dynamical Systems and Bifurcations of Vector Fields, Applied Mathematical Sciences Vol. 42*, Westview Press, February 2002.
6. Krauskopf, B., Osinga, H. M., and Galàn-Vioque, J., *Numerical Continuation Methods for Dynamical Systems*, Springer, 2007.
7. Rankin, J., Coetzee, E., Krauskopf, B. and Lowenberg, M., *Bifurcation and Stability Analysis of Aircraft Turning on the Ground*, AIAA Journal of Guidance, Dynamics and Control, Vol. 32, No. 2, March 2009.
8. Coetzee, E., Krauskopf, B. and Lowenberg, M,. *Application of Bifurcation Methods to the Prediction of Low-Speed Aircraft Ground Performance* AIAA Journal of Aircraft, Vol. 47, No. 4, July – August 2010
9. Thota, P., Krauskopf, B. and Lowenberg, M., *Interaction of Torsion and Lateral Bending in Aircraft Nose Landing Gear Shimmy*, Nonlinear Dynamics, 57(3), 2009.
10. Doedel, E., Champneys, A., Fairgrieve, T., Kuznetsov, Y., Sandstede, B., and Wang, X., AUTO 97 : Continuation and bifurcation software for ordinary differential equations, http://indy.cs.concordia.ca/auto/, May 2001.
11. Coetzee, E.B., Krauskopf, B., Lowenberg, B., "Dynamical Systems Toolbox for MATLAB," https://github.com/ecoetzee/Dynamical-Systems-Toolbox, July 2011
12. Hoerner, S. F., *Aerodynamic Drag*, pp 27–30. Ohio, 1951